Supplement of Ocean Sci., 19, 1083–1106, 2023
https://doi.org/10.5194/os-19-1083-2023-supplement
© Author(s) 2023. CC BY 4.0 License.

Ocean Science Open Access EGU

Supplement of

The Weddell Gyre heat budget associated with the Warm Deep Water circulation derived from Argo floats

Krissy Anne Reeve et al.

Correspondence to: Krissy Anne Reeve (krissy.reeve@awi.de)

The copyright of individual parts of the supplement might differ from the article licence.

S1. Vertical boundary conditions for heat budget integrals

Since we are unable to integrate for the full ocean depth (Argo floats profile the upper 2000 dbar), and most importantly, to the surface of the ocean, due to the high seasonal variability at the surface (Section 2.2), we need to decide on suitable vertical boundaries for the heat budget integrals. However, if we simply select uniform depths for the vertical boundaries, we may include certain features in the TS-profile (e.g., such as the temperature minimum) in some areas of the Weddell Gyre, while excluding them in other regions. Hence, we need to ensure the upper boundary is defined such that Θ_{max} (i.e., the core of WDW) is always fully included in the vertical layer, given that the core of WDW is the primary source of heat to the Weddell Gyre. We also need to avoid incorporating seasonally variable Surface Water and Winter Water (a surface water mass characterised by a sub-surface temperature minimum, e.g., Behrendt et al., 2011). Otherwise, the vertical advection component will be stronger in regions where the profile includes the temperature minimum layer due to a larger vertical temperature gradient, in contrast to regions where the Winter Water is altogether omitted. This will result in bias in the spatial distribution of the heat budget terms. It is also necessary to ensure the same thickness of water is analysed throughout the Weddell Gyre. We resolve this by defining the upper boundary as the mid-point of the thermocline, and the lower boundary as 1000 m below the thermocline mid-point (Fig. 2 & S1). That way, regardless of location, we exclude Winter Water, but always include the core of WDW, and maintain equal layer thickness throughout. An example vertical temperature profile in Fig. 2 illustrates the vertical boundary conditions, while a map of the upper boundary depth is shown in Fig. S1.

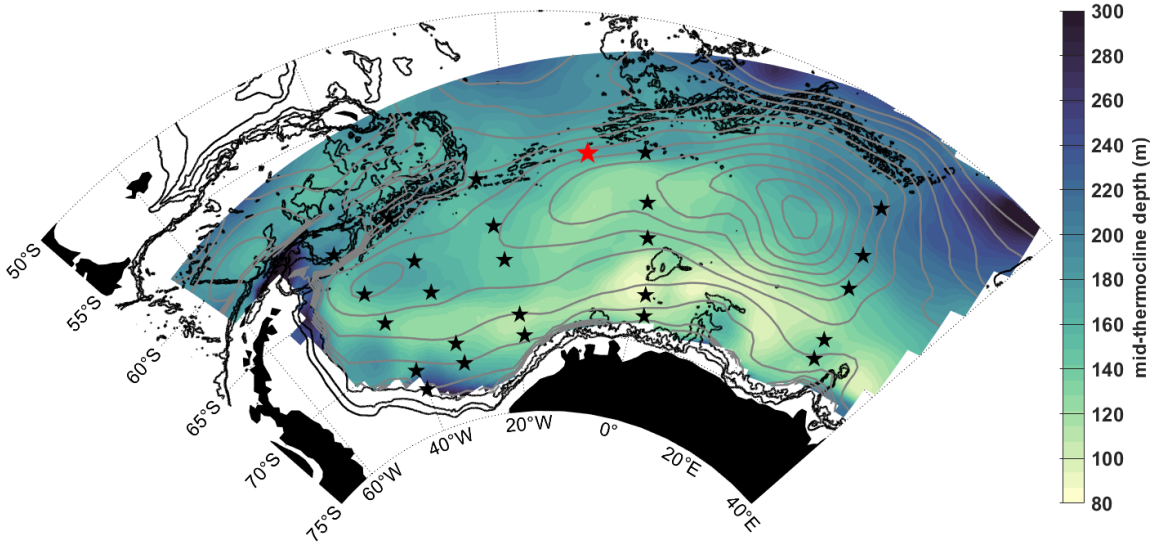

Figure S1: The mid-thermocline, defined as the upper boundary depth (m), with stars marking the positions of profiles plotted in Fig. 2, and streamlines (grey contours) of the vertically integrated stream function for 50-2000 dbar with a spacing of 5 Sv, derived from in-situ observations from Argo floats (Reeve et al., 2019, 2016), as in Fig. 1. The black contours show the 1000, 2000 and 3000 m isobaths, from the general bathymetric chart of the oceans (GEBCO, IOC et al., 2003).

S2. Air-sea-heat fluxes

The net air-sea heat flux is the sum of the following components: shortwave solar radiation, longwave thermal radiation, latent heat flux and sensible heat flux. The air-sea heat fluxes are not directly relevant in the calculation of the heat budget in this study, since the heat budget calculations are restricted to depths exceeding 80 m (i.e., the minimum depth of the mid-thermocline is below 50 m, Fig. S1), and downward shortwave radiation decreases exponentially with depth (only 1% of the radiation reaches past 75 m; Tamsitt et al., 2016). However, gaining perspective on where we expect heat loss through the surface of the ocean may help to understand the mechanisms through which WDW loses its heat as it circulates the Weddell Gyre. Long-term means between 2002 and 2016 of surface heat fluxes are derived from ERA-interim reanalysis (Hersbach et

al., 2020), based on previous convictions that it provides one of the most reliable estimates for the Southern Ocean (Jones et al., 2016). We also use this data source to derive vertical Ekman pumping velocity, as detailed in the following Section S3.

The net air-sea heat flux into the ocean in Fig. S2 (here on referred to as Q_{net}) is positive along the northern limb of the gyre and negative over the southern limb, creating a north-south divide (the thick black line in Fig. S2) parallel to the central gyre axis (the dashed black line in Fig. S2). There is, however, some latitudinal offset between Q_{net} and the central axis of the depth-integrated circulation. Thus, the IC is dominated by positive Q_{net} fluxes, and the zero contour in Q_{net} (thick black line in Fig. S2) appears south of the central gyre axis, roughly between the IC and the SL, instead of directly along the central axis of the gyre.

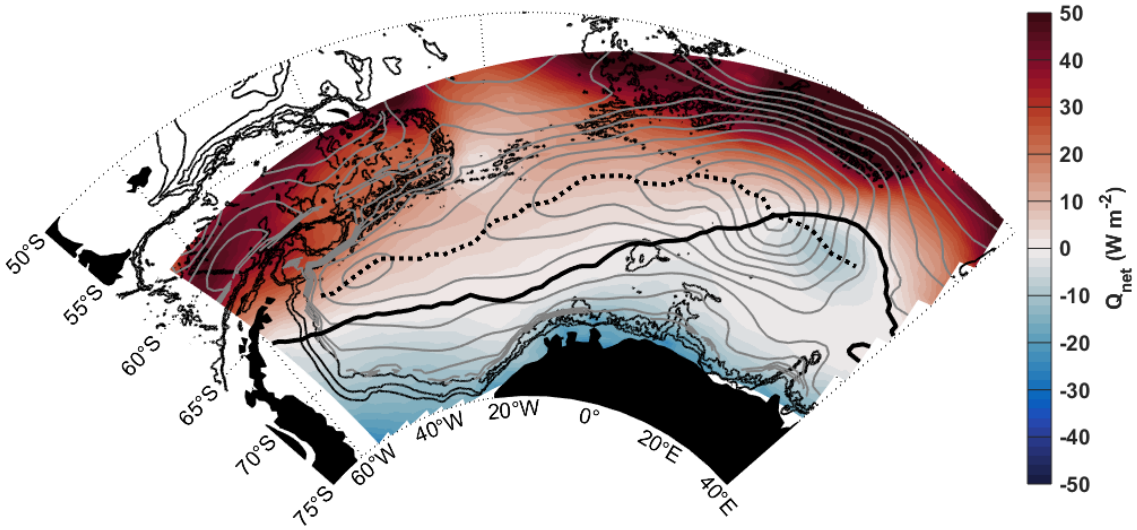

Figure S2: Net air-sea heat flux (i.e., the sum of long/short-wave radiation, latent and sensible heat flues, in W m^{-2}): long-term mean from 2002 to 2016, from ERA-interim reanalysis data. Positive values indicate heat flux into the ocean. The thick black line indicates the zero-contour line for Q_{net}. The central gyre axis is indicated by the dashed black line, defined as the meridional maximum stream function value. South of the dashed line the flow of the water column is westward and flow north of the dashed line is eastward. Streamlines (grey contours) show the vertically integrated stream function for 50-2000 dbar with a spacing of 5 Sv, derived from in-situ observations from Argo floats (Reeve et al., 2019, 2016), as in Fig. 1. The black contours show the 1000, 2000 and 3000 m isobaths, from the general bathymetric chart of the oceans (GEBCO, IOC et al., 2003).

S3. Vertical Ekman pumping velocity derived from the wind stress field

Since the flow is assumed geostrophic (non-divergent), vertical velocity is assumed constant with changing depth (outside of the turbulent surface and bottom boundary layers, which are excluded in this study, see Section S1). As an estimate of the vertical velocity is required in the vertical advection term (the second term on the right-hand side of Eq. 1.1), we therefore use the Ekman vertical velocity, w_E. The Ekman velocity, w_E, was derived from the mean wind stress field, sea ice concentration (α) and sea ice velocity (U_{ice}) for the period 2002-2016, following Le Paih et al. (2020) and Dotto et al. (2018):

$$w_E = \vec{\nabla} \times \left(\frac{\vec{\tau}}{\rho_0 f} \right) \tag{2.1}$$

where

$$\vec{\tau} = \alpha \vec{\tau}_{ice-ocean} + (1-\alpha)\vec{\tau}_{air-ocean} \tag{2.2}$$

$$\tau_{air-ocean} = \rho_{air} C_{dw} \left|\overrightarrow{U_{air}}\right| \overrightarrow{U_{air}} \tag{2.3}$$

and

$$\tau_{ice-ocean} = \rho_0 C_{id} \left|\overrightarrow{U_{ice}}\right| \overrightarrow{U_{ice}} \quad (2.4)$$

where ρ_0 is seawater density (1027 kg m^{-3}) and f is the Coriolis parameter; $\vec{\tau}$ is the total surface stress, which takes into account sea ice concentration, α, by combining stress over the ocean by wind ($\vec{\tau}_{air-ocean}$) and stress over the ocean by ice ($\vec{\tau}_{ice-ocean}$). ρ_{air} is the density of air (1.29 kg m^{-3}), C_{dw} is the wind drag coefficient (1.5x10^{-3}), $\overrightarrow{U_{air}}$ is the wind velocity at 10 m above sea level; C_{id} is the ice-ocean drag coefficient (5.5x10^{-3}) and $\overrightarrow{U_{ice}}$ is the sea ice velocity. The data sources for the variables in Eq. 2 are listed in Table 1, in Section 2.1.

Eq. 2.1 relies on a formulation for wind stress (air-sea momentum flux) of an ice-free ocean. Le Paih et al. (2020) showed that different stress formulations, including sea ice-sensitive ones, in the Weddell Gyre area yield momentum input into the ocean within +/- 10% relative to the formulation used here. Since w_E is assumed to be constant with depth below the Ekman layer (i.e., assuming the horizontal flow below the Ekman layer to be in perfect geostrophic balance), and the surface mixed layer is omitted from the objectively mapped grids of velocity and temperature, w_E is a suitable estimate of the vertical velocity within the scope of this study. The resulting w_E was averaged over 2002-2016 (Fig. S3) and re-gridded to the same grid as the Argo data, using a simple distance-weighted mean. w_E is positive throughout most of the Weddell Gyre (indicative of upwelling), whereas downwelling is found along the Antarctic coastline and on the continental shelf in the south-west, which is excluded from this study since Argo float data are sparse for the shelf seas.

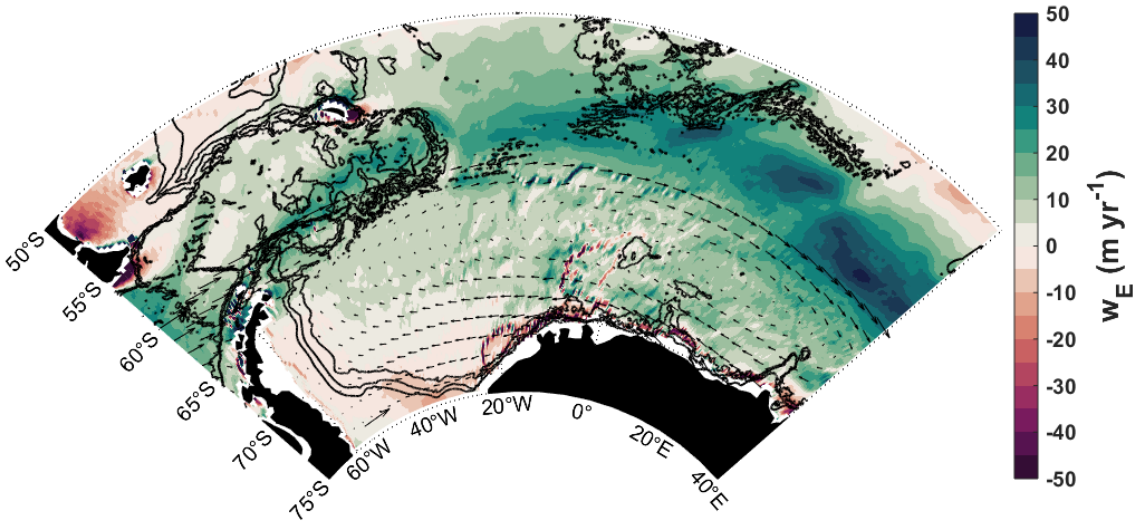

Figure S3: Mean 2002-2016 vertical Ekman pumping velocity (w_E: m/year), from Era-interim ECMWF reanalysis (ERA5 monthly mean output; Hersbach et al., 2020) and sea-ice velocity from Polar Pathfinder Daily 25 km EASE-Grid Sea Ice Motion Vectors (Tschudi et al., 2019), where positive values indicate upwelling. Black arrows show surface wind stress (N m^{-2}), south of 60°S (in order to emphasise the weaker surface wind stress within the Weddell Gyre region, which would disappear if we were to include the much stronger wind stress over the ACC); the arrow at 50°W, 74°S is 0.05 N m^{-2}. The black contours show the 1000, 2000 and 3000 m isobaths, from the general bathymetric chart of the oceans (GEBCO, IOC et al., 2003).

S4. Horizontal diffusivity

In the north and east, we use horizontal diffusivity estimates from Sevellec et al. (2022; 2020). For all data within 1° lat/lon of a grid cell, we take the mean and standard error of the mean (s.e.). For grid cells where no data is available, we use 247 ± 63 m^{2}s^{-1}. The Sevellec et al (2022) dataset might underestimate values within the interior gyre where sea ice dominates, which is why we replaced these values with 247 ± 63 m^{2}s^{-1}, from Donnelly et al. (2017). This is because the authors need ice-free consecutive float positions for an adequate length of time for the implementation of their method, suggesting the data are biased to conditions where the sea ice has melted and the wind has not yet stirred up the water column, leaving a layer of fresh

water over the surface (as occurred, for example, in Cisewski et al., 2011). Also, given the Sevellec dataset is representing 1000 m, whereas the depth range we are looking at varies from 87 to 1530 m, with a mean upper boundary of 166 m, and a mean middle depth of 666 m, we can expect higher values overall for the shallower layer. Maps of the resulting zonal and meridional horizontal diffusivities used in this paper are provided in Fig. S4, along with their corresponding standard errors.

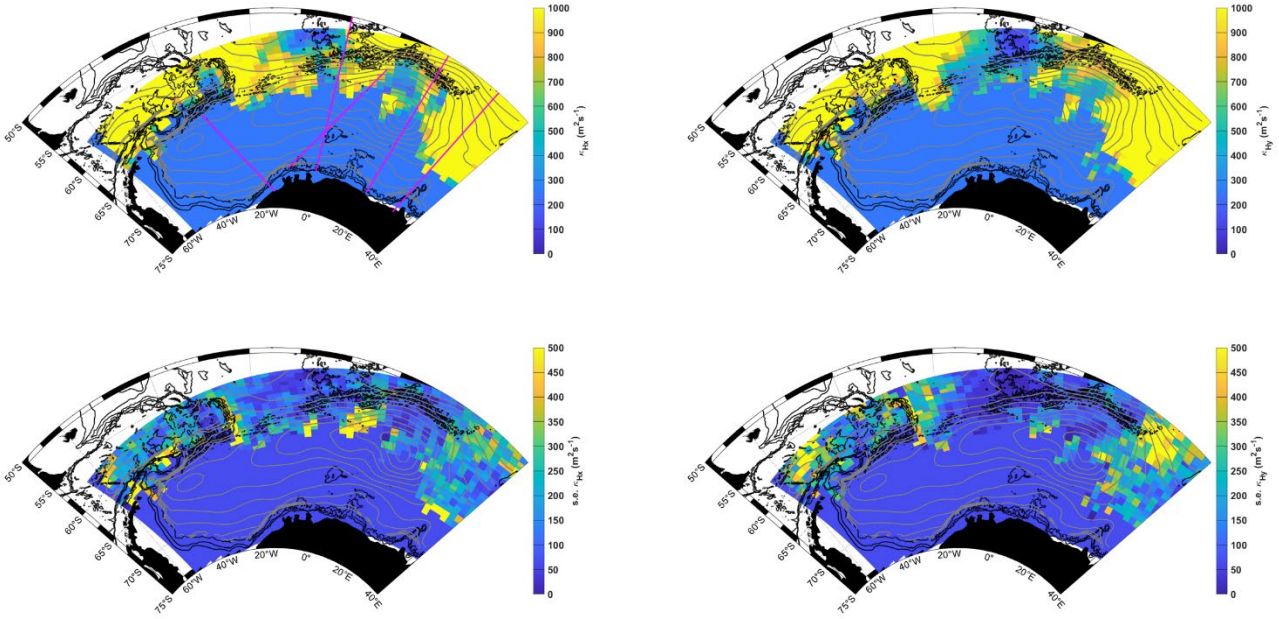

Figure S4: Horizontal diffusivity as a combination of the Sevellec at al. (2022) dataset and infilling with a background value of 247 ± 63 m2s-1 m^2s^{-1}, from Donnelly et al. (2017). The upper panels show the zonal and meridional components from left to right, whereas the lower panels show their corresponding standard errors respectively. In the upper left panel, magenta lines mark the approximate positions of the ship-based data used in Donnelly et al., (2017).

S5. Investigating uncertainty: horizontal gradients

To look into the causes of the large ellipses in the pattern of horizontal heat advection, spread diagonally north-eastwards from Maud Rise (Fig. 3a), we checked the horizontal gradients in the upper boundary depth and the sub-surface temperature maximum, shown in Figs. S5a-b respectively. These have been discussed in Section 5.2.2.

(a)

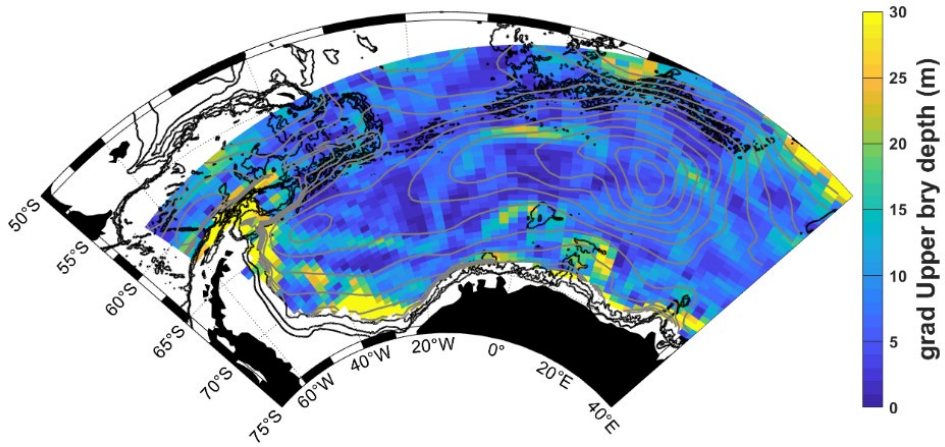

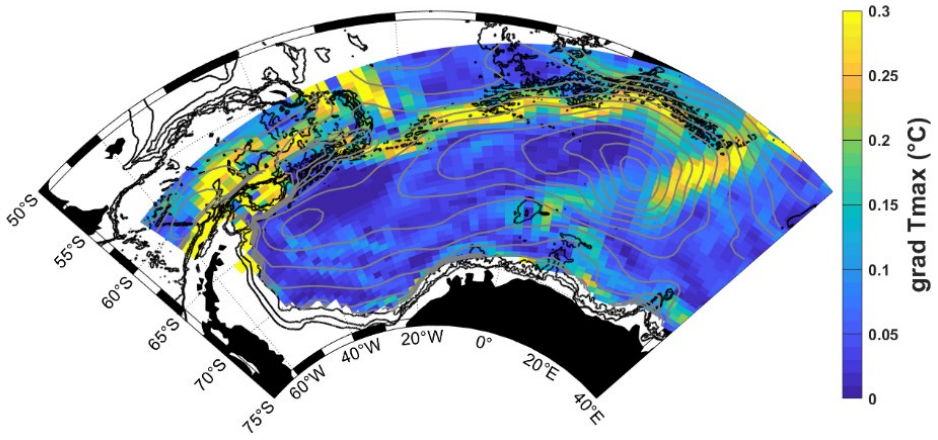

(b)

Figure S5: (a) Horizontal gradient in the upper boundary depth (i.e. mid-thermicline depth; m), and (b) horizontal gradient in the sub-surface temperature maximum (°C).

S6. Diffusive heat fluxes across boundaries

In Section 4.2 we investigate the role of horizontal turbulent diffusion in redistributing heat across zonal boundaries: across the northern boundary of the Weddell Gyre from the ACC (Fig. 7b), across the interface between the open SL and the IC-south (Fig. 9b), and across the central gyre axis between IC-south and IC-north (Fig. 9c). Provided below in Fig. S6 are the zonally integrated diffusive heat fluxes corresponding to each of these regions respectively, from which we derive our net diffusive heat fluxes in Section 4.2.

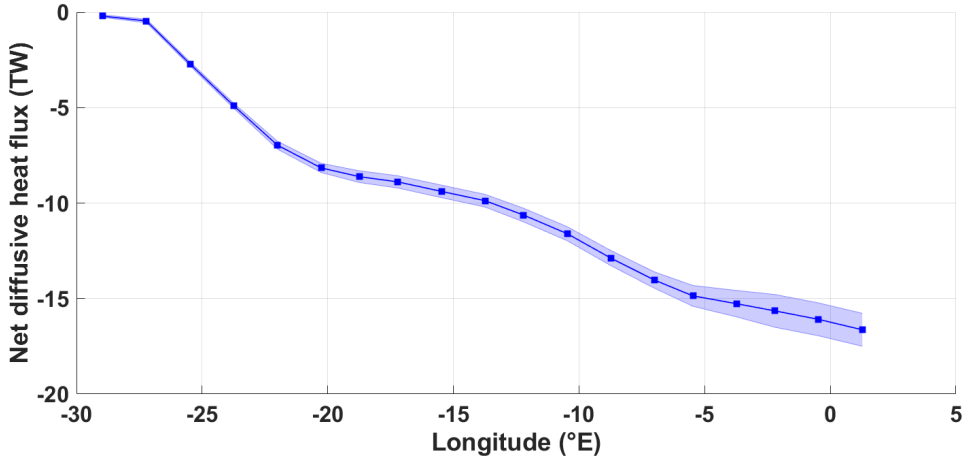

(a)

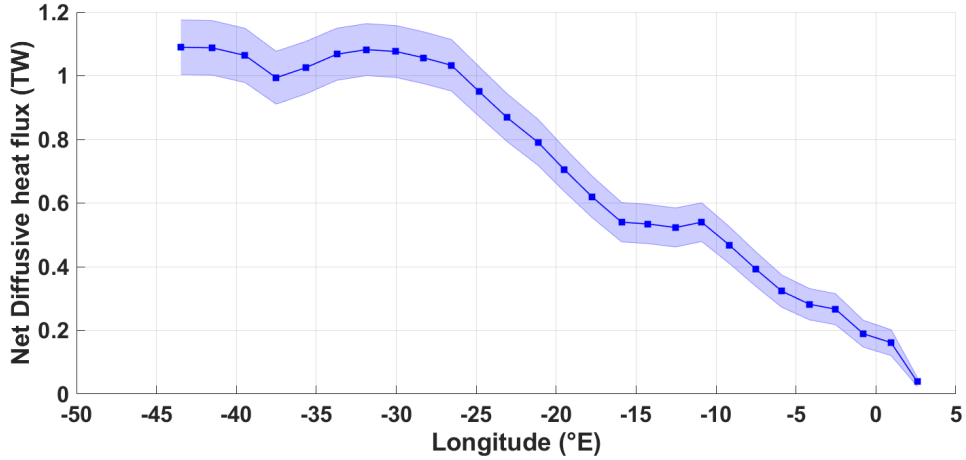

(b)

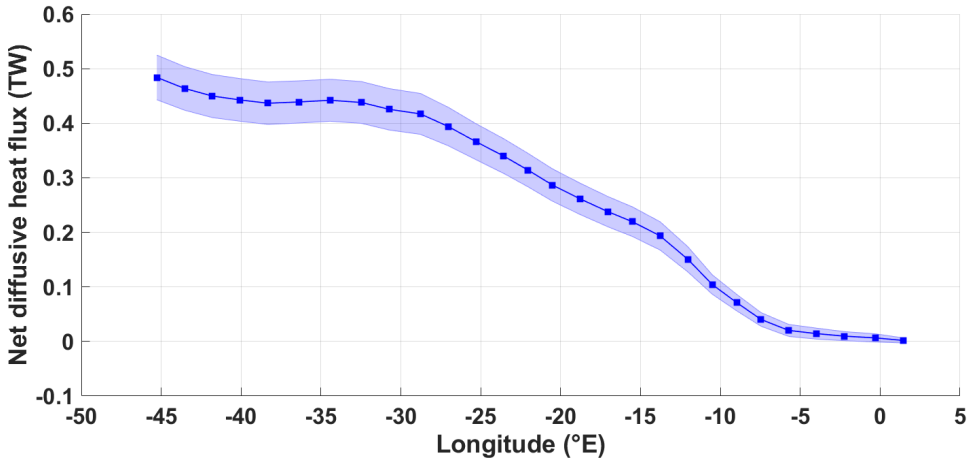

(c)

Figure S6: the cumulative sum of the diffusive heat flux in TW. (a) across the northern gyre boundary from west to east, where negative values indicate a southward flux of heat into the eastward-flowing northern limb of the Weddell Gyre from north of the northern Weddell Gyre boundary; (b) along the boundary between the southern inflow limb and IC-south, from east to west, where positive values indicate a removal of heat from the open southern limb of the gyre into the interior; in other words, a northward flux of heat from the southern limb into the interior circulation cell; (c) across the central gyre axis from IC-south to IC-north, where positive values indicate a diffusive heat flux northwards across the gyre axis. Errors are computed following the same method outlined in Section 3.2 and S7, with the cumulative net error summed in quadrature (i.e., the square root of the cumulative sum of the squared error).

S7. Error propagation computation

The errors for each heat budget term are calculated using the laws of propagation, where the error for temperature is defined as the objective mapping error (Fig. S7; Reeve et al., 2016), and the error for horizontal velocity is provided from Reeve et al. (2019), which contains a sensitivity study, perturbing the original stream function by using mapping errors and uncorrected drift velocities, to get a maximum range of values (see Reeve et al., 2019 for more details). For further details refer to Sections 2.2 and 3.2. The error for w_E are the standard error of the mean of the timeseries variability for monthly values from January 2002 to December 2016, since uncertainties associated with the wind field are as of yet unavailable for ERA-5 reanalysis data. Lastly, we use the error ranges for horizontal and vertical diffusivity as provided in Donnelly et al. (2017), for all regions within the Weddell Gyre, or, where available, the Sevellec et al. (2022) dataset, which also provides error estimates (Section S4). With all this in mind, the derivation for the propagated errors for each term are provided below.

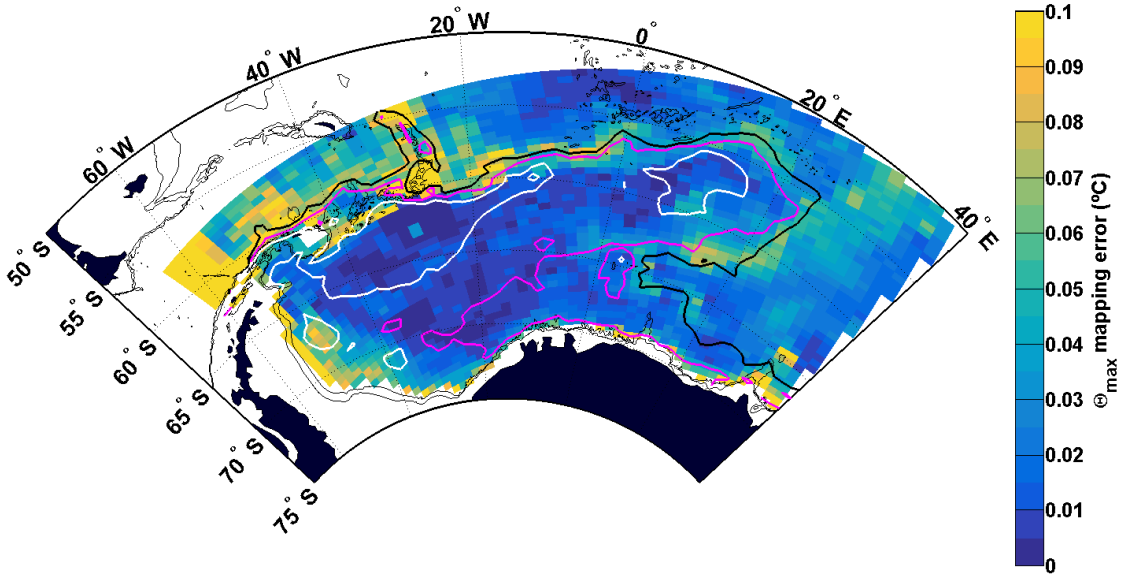

Figure S7: Mapping error for Θ_{max} (°C). The gridded Θ_{max} field is shown in Fig. 1. The white, magenta and black contours show the 0.5, 0.8 and 1.1 °C isotherms respectively. The grey contours are as in Fig. 1.

For any one grid cell, the uncertainty for mean horizontal advection is the propagation of error as applied to two variables multiplied together:

$$\delta A_H = |U\Theta| \cdot \sqrt{\left(\frac{\delta\Theta}{\Theta}\right)^2 + \left(\frac{\delta U}{U}\right)^2 + \frac{2COV(U\Theta)}{|U\Theta|}} \quad \text{(S2.1)}$$

where δ is the uncertainty of a variable, and COV(UΘ) is the covariance between U and Θ, which is $COV(U\Theta) = \rho_{\Theta u}\delta U\delta\Theta$, where $\rho_{\Theta U}$ is the correlation between Θ and U. The resulting uncertainties are propagated using the root-sum-square (RSS) law of error propagation, which is first applied to the differential: $\nabla_H(U \cdot \Theta) = \frac{d(u\Theta)}{dx} + \frac{d(v\Theta)}{dy}$ (the length scales Δx and Δy are also applied). RSS is then applied to the vertical integration for the 1000 m thick layer, and also applied when integrating horizontally over larger areas. RSS is applied when integrating vertically and horizontally in the same way for all terms in Eq.1.1, and the resulting uncertainty of all terms are scaled by ρ_0 and C_p, as well as the associated length scales (Δx and Δy in the horizontal terms, Δz for the vertical terms) as in the heat budget in Eq. 1.2.

For the mean vertical advection term, RSS is applied to the uncertainties of the temperature difference between the upper and lower boundaries, and then this error is propagated with the uncertainty associated with w_E as follows:

$$\delta A_V = |A_V| \cdot \sqrt{\left(\frac{\delta w_E}{w_E}\right)^2 + \left(\frac{\delta T}{T}\right)^2} \quad \text{(S2.2)}$$

where $T = \Theta_{mT} - \Theta_{mT-1000}$, i.e., the temperature difference between the upper and lower boundary (Eq. 1.2), and the resulting uncertainty of T is:

$$\delta T = \sqrt{\delta^2\Theta_{mT} + \delta^2\Theta_{mT-1000}} \quad \text{(S2.3)}$$

Horizontal turbulent diffusion (i.e., the third term on the right-hand side of Eq. 1.1) consists of a double differential of Θ multiplied by κ_H, both of which have an associated uncertainty. The double differential is computed by taking the temperature differences between grid cells (i.e., $\tau = (\Theta_{i-1} + \Theta_{i+1} - 2\Theta_i)/\Delta x^2$, where *i* represents the grid index for one direction; this is

repeated for both x and y directions). Thus, we apply the propagation of error to the uncertainty of the double differential using RSS (i.e., we sum together the square of 12 uncertainties for temperature, which include 2^2 x grid cell *i*, plus its surrounding grid cells, *i*-1 and *i*+1, which is repeated in both *x* and *y* directions, and then scaled by $\Delta X^2 = \Delta x^2 = \Delta y^2$; Eq. S2.5). We then take that uncertainty and apply the propagation of error for two variables multiplied together to incorporate the uncertainty for κ_H (Eq. S2.4). The vertical and horizontal integrations are treated using RSS, as above.

$$\delta D_H = |\kappa_H \nabla_H^2 \theta| \cdot \sqrt{\left(\frac{\delta \kappa_H}{\kappa_H}\right)^2 + \left(\frac{\delta \tau}{\tau}\right)^2} \tag{S2.4}$$

$$\text{Where } \delta\tau = \sqrt{\frac{12\delta\tau^2}{\Delta X^2}} \tag{S2.5}$$

Lastly, vertical turbulent diffusion is treated in the same manner as horizontal turbulent diffusion, except that it is applied in the vertical (i.e., the horizontal operator is not required when computing this term), and thus vertical integration is already accounted for:

$$\delta B = \frac{\sqrt{4\delta\theta^2}}{|B|} \tag{S2.6}$$

$$\text{where } B = \left(\frac{d\theta}{dz}\right)_{mT} - \left(\frac{d\theta}{dz}\right)_{mT-1000} \tag{S2.7}$$

The resulting propagated error is then:

$$\delta D_V = |\kappa_V B| \cdot \sqrt{\left(\frac{\delta \kappa_V}{|\kappa_V|}\right)^2 + \left(\frac{\delta B}{B}\right)^2} \tag{S2.8}$$

Lastly, the net uncertainty of the sum of the heat budget terms is the RSS of the uncertainty of all 4 terms described above:

$$\delta_{HB} = \sqrt{{\delta A_H}^2 + {\delta A_V}^2 + {\delta D_H}^2 + {\delta D_V}^2} \tag{S2.9}$$

The panels on the right side in Fig. 3 show the total propagated errors for the 4 heat budget terms and the sum of all terms respectively. The overall error is dominated by the mean horizontal advection term (Fig. 3a), and to a slightly lesser extent the horizontal turbulent diffusion term (Fig. 3c), with largest errors occurring to the north of the gyre and also over the eastern sub-gyre, particularly east of about 20° E. This is to be expected as this region is dominated by a mesoscale eddy field (Ryan et al., 2016; Schröder & Fahrbach, 1999), while also lacking in observations to adequately represent the long-term mean of the region's hydrography and circulation. The gyre periphery has the largest errors for the horizontal turbulent diffusion term, which corresponds to regions with sharp lateral temperature gradients and large objective mapping errors (Reeve et al., 2016), such as towards the southern coastline, where data are also lacking, and at the northern boundary of the gyre, where high temporal variability is known and sharp meridional temperature gradients are found. For further discussion regarding uncertainty, refer to Sections 5.1 & 5.2.2.

S8. Zonal and meridional variation of the heat budget terms for the whole western Weddell Gyre

The zonal and meridional means and integrations for the whole Weddell Gyre region west of Maud Rise (i.e., SL + IC) were also computed for the heat budget terms. These figures are shown below. The zonal mean in Fig. S8 is very similar to the IC analysis, although it shows a net zero contribution of mean advection, which makes sense because of the gyre-characteristics of the circulation, where westward flowing southern and eastward flowing northern limbs cancel with each other: heat is advected into the gyre east of 10 °E, and then advected out of the gyre west of 40 °W. Horizontal turbulent diffusion dominates as a heat source east of ~25 °W, dominated by high values along the northern boundary. The mean contributions in the upper panel show three zonal peaks at 0 °E, 20 °W and 45 °W. These are related to the recirculation about the eastern sub-gyre, and the western sub-gyre respectively. The peak at 20 °W is particularly interesting as this is where the bottom bathymetry transitions from complex in the east to smooth in the west, which is known to impact diffusivity (Whalen et al., 2012) and overall circulation dynamics (Sonnewald et al., 2023).

The meridional mean in Fig. S9 also shows the closure of the mean advection component where the main heat source due to mean advection occurs in the southern limb (south of ~63°S) and the main heat sink due to mean advection occurs in the northern limb (north of ~63°S). Again, this agrees with all previous findings in the paper. Horizontal turbulent diffusion removes heat in the southern limb, and becomes a source of heat in the northern limb, with peaks occurring at ~61°S and ~59°S. These peaks might be related to the meridional change in the northern boundary across the area we are averaging over.

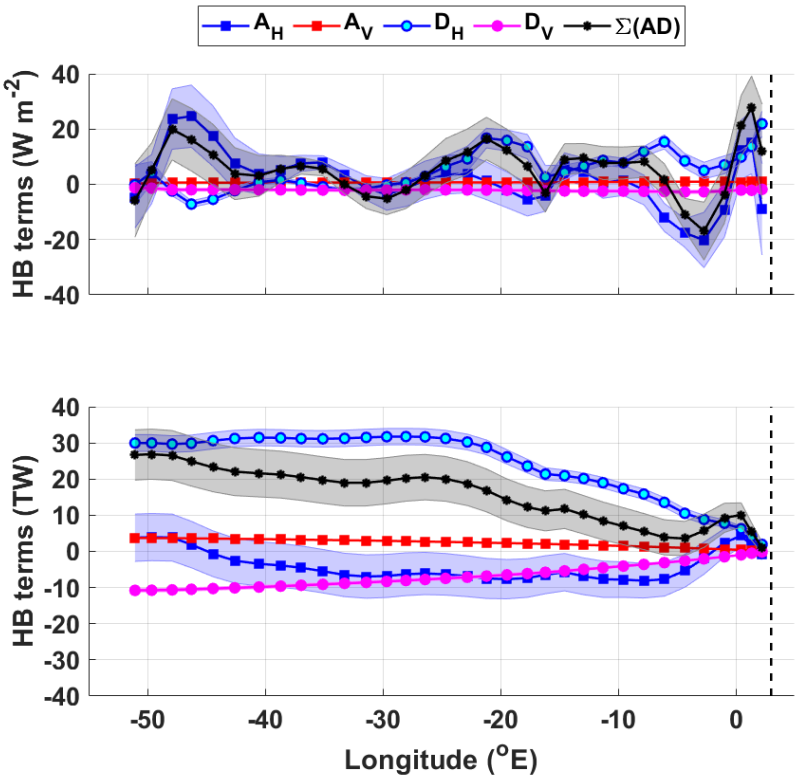

Figure S8: upper panel: the zonal mean heat budget terms, in Wm^{-2}, for the whole Weddell Gyre west of 3 °E; lower panel: the corresponding cumulative heat budget terms in Terawatts (TW). The key for the legend is listed in Table 2. The dashed vertical line marks the approximate longitude of Maud Rise, at 3° E. The shaded errors provide the associated propagated error (detailed in section 3.2 and the supplement). The total region is marked by both blue and magenta stippling in Fig. 4.

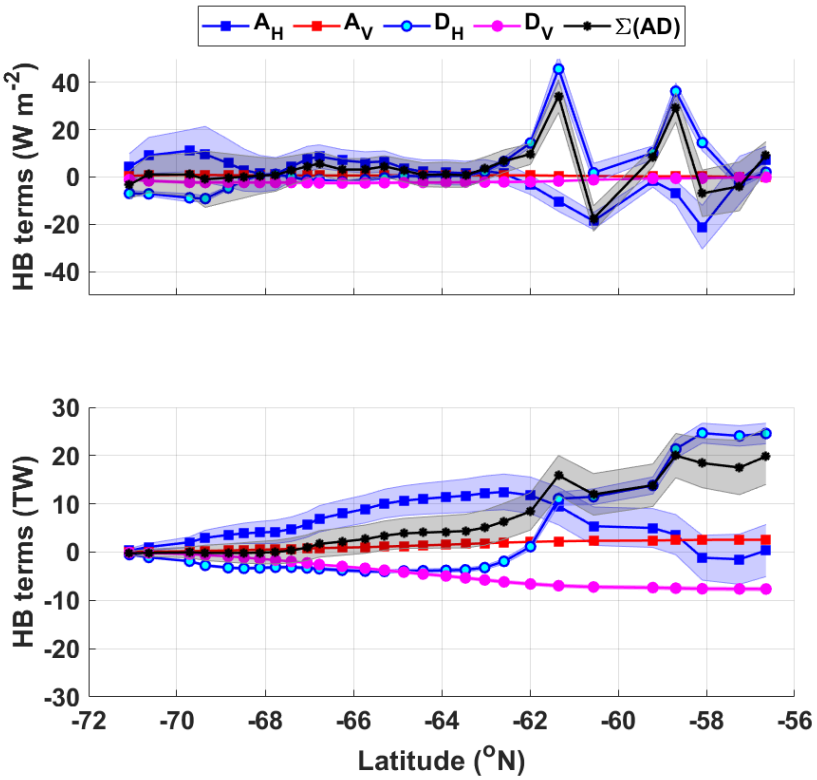

Figure S9: upper panel: the meridional mean heat budget terms, in Wm^{-2}, for the whole Weddell Gyre west of 3 °E; lower panel: the corresponding cumulative heat budget terms in Terawatts (TW). The key for the legend is listed in Table 2. The dashed vertical line marks the approximate longitude of Maud Rise, at 3° E. The shaded errors provide the associated propagated error (detailed in section 3.2 and the supplement). The total region is marked by both blue and magenta stippling in Fig. 4.

S9 References

Behrendt, A., Fahrbach, E., Hoppema, M., Rohardt, G., Boebel, O., Klatt, O., Wisotzki, A., and Witte, H.: Variations of winter water properties and sea ice along the Greenwich Meridian on decadal time scales, Deep-Sea Research Part II, 58, 2524–2532, doi:10.1016/j.dsr2.2011.07.001, 2011.

Cisewski, B., Strass, V.H., and Prandke, H.: Upper-ocean vertical mixing in the Antarctic Polar Front Zone, Deep-Sea Research II, 52:1087–1108. doi:10.1016/j.dsr2.2005.01.010, 2005.

Donnelly, M., Leach, H. and Strass, V.: Modification of the deep salinity-maximum in the Southern Ocean by circulation in the Antarctic Circumpolar Current and the Weddell Gyre. Ocean Dynamics, 67(7), pp.813-838, 2017.

Dotto, T.S., Naveira Garabato, A., Bacon, S., Tsamados, M., Holland, P.R., Hooley, J., Frajka-Williams, E., Ridout, A. and Meredith, M.P.: Variability of the Ross Gyre, Southern Ocean: Drivers and responses revealed by satellite altimetry. Geophysical Research Letters, 45(12), pp.6195-6204, 2018.

Hersbach, H., Bell, B., Berrisford, P., Hirahara, S., Horányi, A., Muñoz-Sabater, J., Nicolas, J., Peubey, C., Radu, R., Schepers, D., Simmons, A., Soci, C., Abdalla, S., Abellan, X., Balsamo, G., Bechtold, P., Biavati, G., Bidlot, J., Bonavita, M., De Chiara, G., Dahlgren, P., Dee, D., Diamantakis, M., Dragani, R., Flemming, J., Forbes, R., Fuentes, M., Geer, A., Haimberger, L., Healy, S., Hogan, R.J., Hólm, E., Janisková, M, Keeley, S., Laloyaux, P., Lopez, P., Lupu, C., Radnoti, G., de Rosnay, P., Rozum, I., Vamborg, F., Villaume, S., Thépaut, J.: The ERA5 global reanalysis. Q J R Meteorol Soc. 146: 1999– 2049. https://doi.org/10.1002/qj.3803, 2020.

IOC, IHO, and BODC: The GEBCO_2014 Grid, version 20150318, on behalf of the Intergovernmental Oceanographic Commission and the International Hydrographic Organization as part of the General Bathymetric Chart of the Oceans, British Oceanographic Data Centre, Liverpool, UK, http://www.gebco.net, [data set], 2003.

Jones, R. W., I. A. Renfrew, A. Orr, B. G. M. Webber, D. M. Holland, and Lazzara, M. A.: Evaluation of four global reanalysis products using in situ observations in the Amundsen Sea Embayment, Antarctica, J. Geophys. Res., Atmosphere, 121, 6240–6257, doi: 10.1002/2015JD024680, 2016.

Le Paih, N., Hattermann, T., Boebel, O., Kanzow, T., Lüpkes, C., Rohardt, G., Strass, V. and Herbette, S.: Coherent seasonal acceleration of the Weddell Sea boundary current system driven by upstream winds. Journal of Geophysical Research: Oceans, 125(10), p.e2020JC016316, https://doi.org/10.1029/2020JC016316, 2020.

Reeve, K. A., Boebel, O., Kanzow, T., Strass, V., Rohardt, G. and Fahrbach, E.: A gridded data set of upper-ocean hydrographic properties in the Weddell Gyre obtained by objective mapping of Argo float measurements, Earth Syst. Sci. Data, 8(1), pp. 15-40, 2016.

Reeve, K. A., Boebel, O., Strass, V., Kanzow, T., Gerdes, R.: Horizontal Circulation and volume transports in the Weddell Gyre derived from Argo float data, Progress in Oceanography, 175, pp. 263-283, https://doi.org/10.1016/j.pocean.2019.04.006, 2019.

Ryan, S., Schröder, M., Huhn, O., and Timmermann, R.: On the warm inflow at the eastern boundary of the Weddell Gyre, Deep-Sea Res. I, 107, 70-81, https://doi.org/10.1016/j.dsr.2015.11.002, 2016.

Schröder, M. and Fahrbach, E.: On the structure and the transport of the eastern Weddell Gyre. Deep Sea Res. Part II: Topical Studies in Oceanography, 46(1-2), pp.501-527, 1999.

Sévellec F., Verdière A.C. d., Kolodziejczyk N.: Deep Horizontal Turbulent Diffusivity. SEANOE. https://doi.org/10.17882/91335, [data set], 2020.

Sévellec, F., Verdière, A. C. d., & Kolodziejczyk, N. Estimation of Horizontal Turbulent Diffusivity from Deep Argo Float Displacements, J. Physical Oceanography, 52(7), 1509-1529, https://doi.org/10.1175/JPO-D-21-0150.1, 2022.

Sonnewald, M., Reeve, K.A. & Lguensat, R.: A Southern Ocean supergyre as a unifying dynamical framework identified by physics-informed machine learning. Commun Earth Environ 4, 153, https://doi.org/10.1038/s43247-023-00793-7, 2023.

Tamsitt, V., Talley, L.D., Mazloff, M.R., and Cerovecki, I.: Zonal Variations in the Southern Ocean heat budget, J. Climate, 29, 6563-6579, doi:10.1175/JCLI-D-15-0630.1, 2016.

Tschudi, M., Meier, W. N., Stewart, J. S., Fowler, C., and Maslanik, J.: Polar Pathfinder Daily 25 km EASE-Grid Sea Ice Motion Vectors, Version 4. Boulder, Colorado USA. NASA National Snow and Ice Data Center Distributed Active Archive Center. https://doi.org/10.5067/INAWUWO7QH7B, [data set], 2019.

Whalen, C. B., Talley, L. D., and MacKinnon, J. A. (2012), Spatial and temporal variability of global ocean mixing inferred from Argo profiles, Geophys. Res. Lett., 39, L18612, doi:10.1029/2012GL053196.